

2018 Spring Technical Meeting
Central States Section of the Combustion Institute
May 20-22, 2018
Minneapolis, Minnesota

Fundamental Study of a 7-element fuel injector configuration for gas turbine combustors, a look at cold flow and burning measurements

Yolanda R. Hicks^{1}, Tyler G. Capil¹, Robert C. Anderson¹, and Kathleen M. Tacina¹*

*NASA Glenn Research Center, Cleveland Ohio, USA
Corresponding Author Email: yolanda.r.hicks@nasa.gov

Abstract: As part of a parametric study in which we vary swirler angle and orientation and look at their effect on fluid mixing and combustion, we examine one configuration of a 7-point lean direct injector by looking at the non-combusting 2-D velocity field using PIV, and combustor system for chemical species using chemiluminescent imaging and flame spectroscopy. The circular 7-point array consists of axial swirlers, with the center 60° counterclockwise swirler surrounded by six 52° clockwise swirlers. The velocity results for this configuration show that the outer swirlers serve to isolate the center flow field near the injector exit. A recirculation zone forms downstream of the center swirler, but not behind the outer swirlers. The combustor results also show an isolated zone directly downstream of the center injector. The flame spectra show variation in speciation of combustion species such as OH* and CH*, and as a function of position within the combustor.

Keywords: *fuel-air mixing, lean direct injection, combustor aerodynamics, PIV*

1. Introduction

Lean Direct Injection (LDI) applied to gas turbine combustors is a strategy is to inject and mix the fuel and air sufficiently in time and space to avoid near-stoichiometric burning that would lead to high NO_x. NASA has used LDI successfully through several programs to reduce fuel burn and emissions [1-4], and because it employs several smaller elements to encompass the area used by more conventional fuel/air mixers, LDI is suited for use in smaller core engines.

To gain a fuller understanding of fluid mixing, fuel vaporization, interaction between the individual elements on the ensuing combustion, we began a parametric study using a 7-element lean direct injector circular array, by varying air swirler angle and center element offset through measurements of velocity, dynamic pressure, and combustion species. References [5] and [6] highlight past work of this parametric study in which we varied swirler angle and element spacing. Reference [7] provides some insight into differences in fields generated using different axial swirler angles.

This paper highlights recent results from the on-going parametric study. We describe the flow from a single swirler configuration, consisting of a central left-hand, 60° swirler, surrounded by six, right-hand 52° swirlers.

2. Methods / Experimental

2.1 LDI hardware

The top of figure 1 shows the components of the LDI element used in these experiments. The air passes through a swirler just before entering a converging-diverging venturi. The air swirlers have an outer diameter of approximately 22-mm, and consist of six helical blades, either right- or left-handed, to generate clockwise or counter-clockwise swirl. The air swirlers used in this study had vane angles of 60° or 52° . At the venturi throat, fuel is injected using a simplex nozzle. This pressure-swirl atomizer was designed to produce a hollow cone spray with a spray angle near 70° . It has a flow number, FN_{US} of about 0.7. A schematic drawing of the 7-point LDI array is shown at the bottom of figure 1. It consists of a center LDI element, surrounded by six elements of equal size. The spacing between adjacent elements is the same, 23.8-mm.

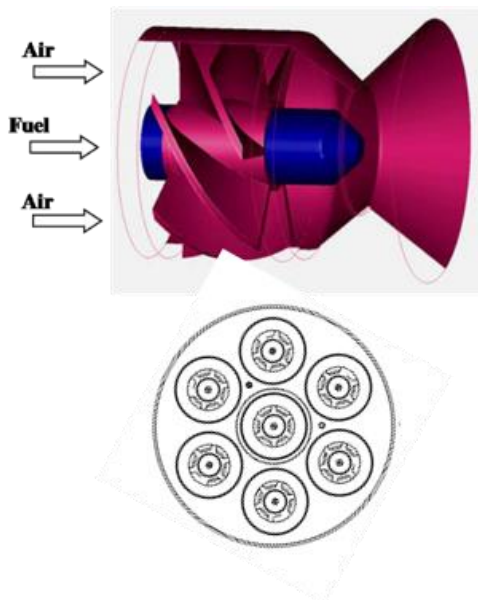


Figure 1: Detail view of a single LDI element; plan view of the 7-point array.

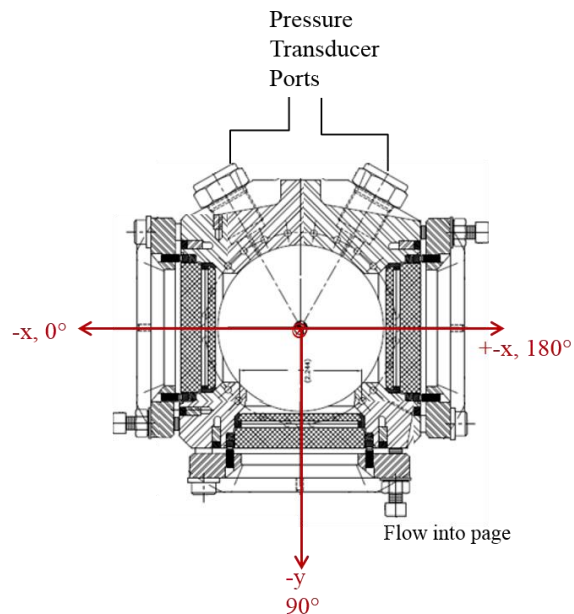


Figure 2: Cross-sectional detail of the combustor that shows the window orientation, defines the coordinate system and shows the locations of the pressure transducer ports

2.2 Test Facility

The experiments were conducted in the Combustion and Dynamics Facility (CDF), in which the flow passes from top to bottom. The combustor test section is 15-cm long with cross-section 7.62-cm in diameter. Three sets of double-paned windows, spaced 90° apart around its circumference, provide optical access to the water-cooled combustor. The windows are flat and have a small offset away from the combustor circumference. The windows measure 6.1-cm tall (axial direction) by 5.8-cm wide (azimuthal). Figure 2 shows a plan view of the combustor section, and the coordinate system definition.

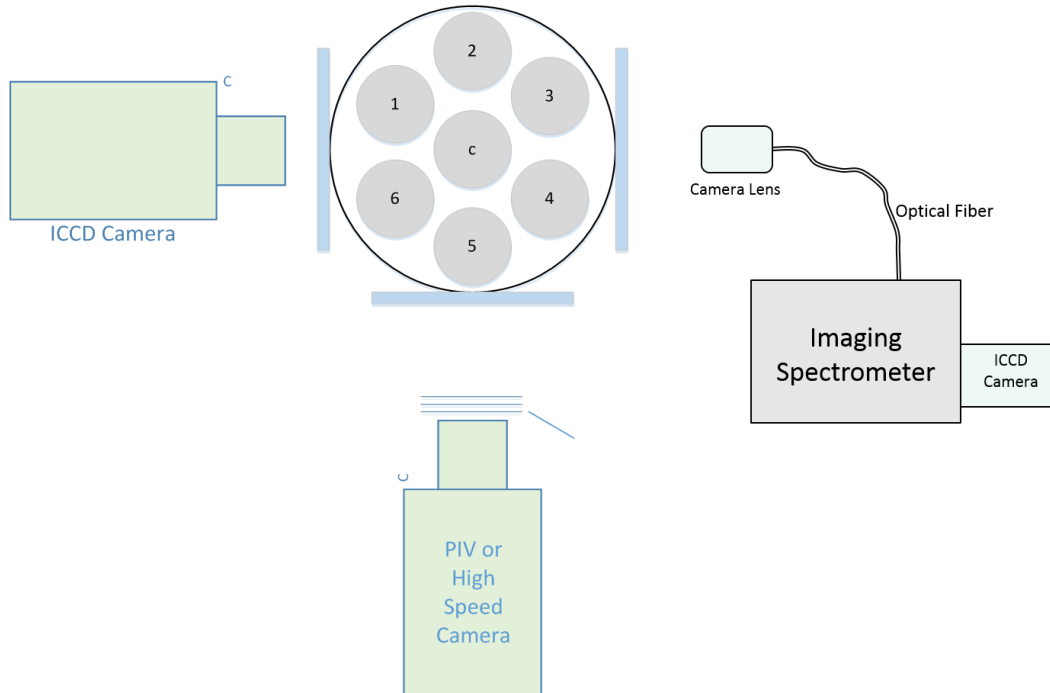


Figure 3: Sketch showing a top view of the imaging system layout and swirler designation and arrangement with respect to the cameras.

2.3 Instrumentation and Procedure

We used an imaging layout like that illustrated in Figure 3. Velocity measurements were obtained using PIV, under non-combusting conditions at the same inlet temperature as the combusting test. For the combusting tests, we collected chemiluminescence from the flame of OH^* , CH^* and C_2^* .

The PIV data were acquired using a 15-Hz, dual-head, frequency-doubled, Nd:YAG laser and a single, interline transfer, CCD camera. The laser beam was formed into a light sheet using a set of cylindrical lenses. The sheet passed through the test section and was aligned parallel with the flow direction. The camera was positioned normal to the laser sheet and collected the light scattered by droplets.

Seeding was achieved using water spray from the center nozzle. This enabled us to heat the air to inlet temperatures we would normally use for combustion tests and match either the volume flow or mass flow rate of the fuel. The advantage of this approach is that the windows stayed clean for the hour or more required to collect the data. Thus, water seeding is far superior to powder or oil seeding. The biggest disadvantage of this approach is that the “seed” is not necessarily uniformly distributed and that in the near field, the water tracks the flow from the nozzle(s) rather than of the air. However, we determined when comparing data from the seeding approaches that using water gave us the information we were looking for in terms of the bulk fluid motion.

We traversed across the flow, typically in 1-mm increments, collecting 500 image pairs per position. Data were collected at 5-bar, 700K, and two cold flow reference velocities, u_{ref} : 22.9-m/s and 15.2-m/s.

For flame chemiluminescence imaging, we used two different cameras. Time-resolved measurements of C_2^* and CH^* were obtained using a 12-bit, high speed CMOS camera ($1k \times 1k$) focused on the vertical center x-z plane at $y=0$. Imaging occurred through the same window as used for the PIV data. We framed at 40,000 per second (exposure time 25- μ s), with resolution of 320×368 pixels, using an $f = 50$ -mm, $f/1.2$ lens. We used a filter wheel to isolate either C_2^* at 514-nm or CH^* at 420-nm. We collected at least 40,000 images per inlet condition, per species. We also obtained C_2^* , CH^* , and OH^* images using an ICCD camera, using frame rate of 20-Hz to collect 500 instantaneous $1k \times 1k$ images per species. We used a gate time of 500-ns per image.

We collected flame spectra using an $f = 105$ -mm, $f/4$, UV lens, coupled to a linear fiber array matched end-to-end. The opposite end transmitted the light to an $f=300$ -mm imaging spectrometer. We used a 300-groove/mm grating blazed at 300-nm. Five grating angles were used to cover the range from 250-nm to 800-nm using a step-and-glue function in the spectrometer control software. The dispersed light was focused onto a gated ICCD camera with a UV intensifier. The fiber was oriented vertically, aligned to the flow direction. The total height imaged was approximately 20-mm. The region of the camera array that was illuminated was binned into 27 strips of equal height. For data collection, we obtained ten individual frames at each grating angle, which can be processed individually or averaged. The gate used for each exposure was 100- μ s. We traversed across the flow horizontally (y-) in 6-mm increments. To span the full window height, we used three vertical positions, spaced 16-mm apart.

2.4 Test matrix

All data were obtained using the same inlet temperature and pressure of 800K, 5-bar. This report focuses on the cases that used even fuel burning, that is, the center swirler and outer swirlers were fueled to have the same equivalence ratio, ϕ . The matrix of burning conditions included air flows that were bounded by the low and middle reference velocities used with PIV. Two variations were included: one that held ϕ constant while varying the cold flow reference velocity; the other that held the reference velocity constant and varied ϕ . Table 1 summarizes the conditions reported on in this paper.

Table 1: Test matrix of inlet conditions that shows the variations for observing effects of reference velocity and equivalence ratio.

Cold flow	u_{ref} , m/s	7.6	15.2	22.9	Constant: $\phi \cong 0.35$	
Burning	u_{ref} , m/s	9.1	10.7	12.2	13.7	Constant: $\phi = 0.45$
	ϕ	0.43	0.45	0.48	0.50	Constant: $u_{ref} = 10.7$ m/s

3. Results and Discussion

We first describe the cold flow 2D velocity fields, then describe some combustng results.

3.1 Cold Flow Velocity Fields

Figures 4 and 5 show the mean 2D velocity field for the three reference velocities, left to right, of 7.6-m/s, 15.2-m/s, and 22.9-m/s. Figure 4 shows the mean horizontal-vertical (axial) vector components at $y=0$, plotted on the same scale. Flow passes from top to bottom. In addition to the 2D-vector field, the top row shows the axial velocity contour, while the bottom row depicts the

RMS of the axial velocity using red squares. Figure 5 shows the axial velocity contours in a slice located near $z = 10$ -mm from the injector exit plane (dump plane).

Considering the mean fields shown in figure 4, only the highest reference velocity shows a distinct central recirculation zone (CRZ) downstream from the center element, at $x = 0$. The mid-point reference velocity presents very low magnitude CRZ, while the lowest reference velocity case shows no CRZ. Because we seed the system by spraying water through the center nozzle, these results in the near field reflect the combination of water drop velocity and air velocity, though they are perhaps more representative of what we would see near the dump plane during combustion. One drawback to this approach is that better atomization is achieved with higher fuel pressure drop, which favors the higher reference velocities. At the lowest air flow rate, we necessarily had to flow water at a higher rate to maintain steady flow, so the local “equivalence ratio” for that condition is higher than 0.35.

The end view slices (figure 5) at $z = 10$ have circles that show the relative positions of the swirlers. The center swirler is dotted to indicate its swirl direction is counter to the outer swirlers. All three fields show high downstream velocity occurs on the side of the outer swirlers closest to the centerline. The lowest reference velocity shows higher velocity directly in the center, but a reverse or stagnant region in the hexagonal gape between the swirlers. The reverse flow zone collapses to the center for the middle reference velocity and increases in strength at the highest reference velocity.

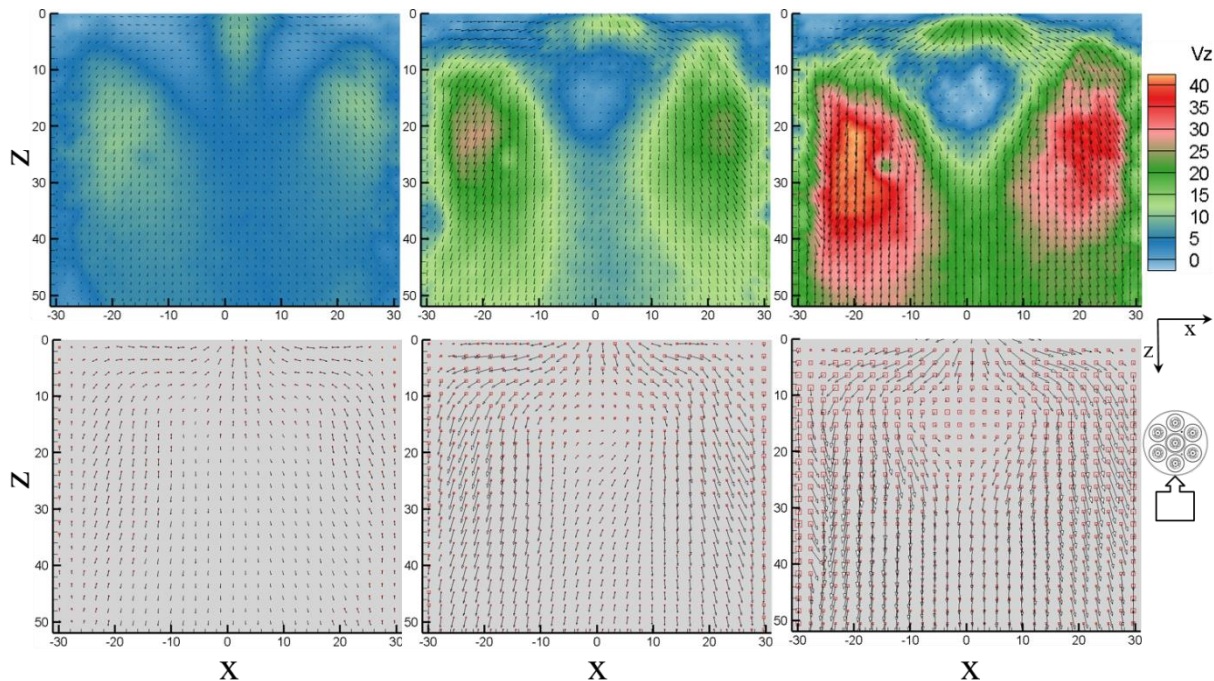


Figure 4: Reference velocity comparison using PIV showing the mean 2D velocity field results of axial velocity at $Y=0$ for u_{ref} (from left) of 7.6, 15.2, and 22.9-m/s. Top: axial-horizontal vectors and axial velocity contour. Bottom: velocity vectors along with squares with size that represents the RMS velocity magnitude.

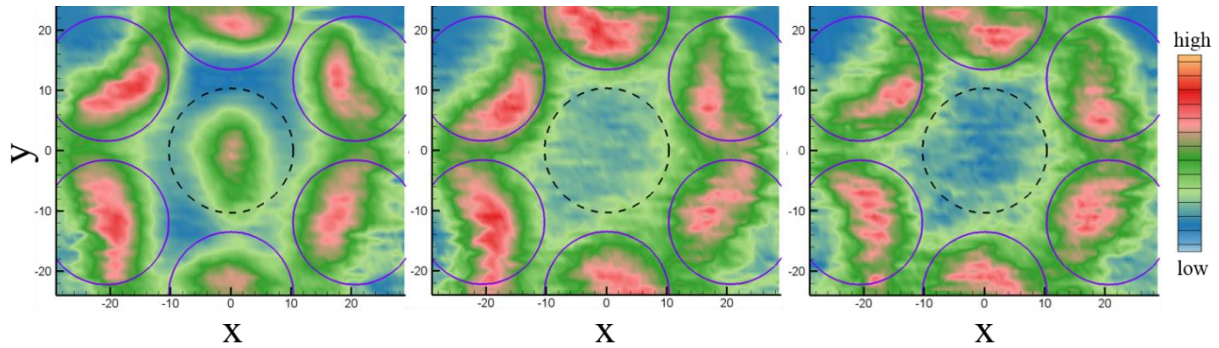


Figure 5: Reference velocity comparison. Axial velocity contours at $\sim z = 10$ -mm, for 7.6, 15.2, and 22.9-m/s. Each is scaled independently.

3.2 Combusting results

3.2.1 Chemiluminescence imaging

In this section, the images are presented as if we are observers in the field looking through the windows. Thus, the images from the ICCD camera show the horizontal axis with $-y$ to the right. Figures 6 and 7 show C_2^* image statistics obtained using the high speed and ICCD cameras, respectively with respect to equivalence ratio, which increases from left to right, for $\phi = 0.43$ to $\phi = 0.50$. The reference velocity is 10.7 m/s. The top row shows the mean signal plotted on the same scale, and the bottom row shows the RMS signal, each scaled individually.

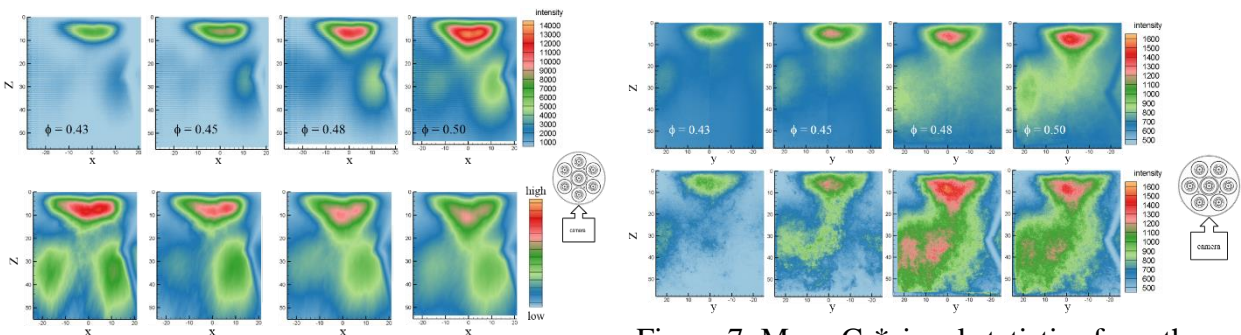


Figure 6: Mean C_2^* signal statistics from the high speed camera, showing variation based on equivalence ratio, which increases from left to right. Top row: mean signal, same scale. Bottom row: signal RMS, scaled independently.

Figure 7: Mean C_2^* signal statistics from the ICCD camera, showing variation based on equivalence ratio, which increases from left to right. Top row: mean signal, same scale. Bottom row: signal RMS, scaled independently.

As expected, C_2^* intensity increases with equivalence ratio. For any given field, the highest signal occurs immediately downstream from the dump plane and about the center (x - or y - =0) from both camera perspectives. This area is also relatively symmetric about the centerline. As ϕ increases, the area becomes more distinctly triangular in shape. Farther downstream, at approximately $z = 20$ -mm, the C_2^* emissions appear asymmetric with respect to the center position of x or $y = 0$. The images from the high speed camera show increasingly strong signal on the position x -side (RHS) of the images, whereas the stronger signal is on the positive y side (LHS) for the ICCD camera. The corresponding RMS images from each camera highlight the structures noted above. Currently, we do not know why the asymmetry exists. One thought is that the swirling flow carries C_2 towards each camera on those sides with high signal, and away from the camera on the lower signal side.

Figures 8 and 9 show the comparison of C_2^* intensity statistics as a function of reference velocity, from low to high, keeping the equivalence ratio constant at 0.45. For these, we see that the overall signal decreases with increasing reference velocity. This result initially seems counterintuitive because the fuel flow rate must increase along with the air flow in order to maintain the same equivalence ratio. However, as mentioned in the cold flow discussion, the higher flow rates require a higher pressure drop across the simplex nozzles, which in turn provides for better fuel atomization and fuel vaporization. The higher air flow rates also lead to higher turbulence intensity and increased fuel-air mixing. It is therefore likely that at the lowest reference velocity, larger droplets exist—consistent with the PIV result—which may still in be in the liquid state. The number density is then greater and results in the highest chemiluminescence signal, despite having the lowest overall amount of fuel.

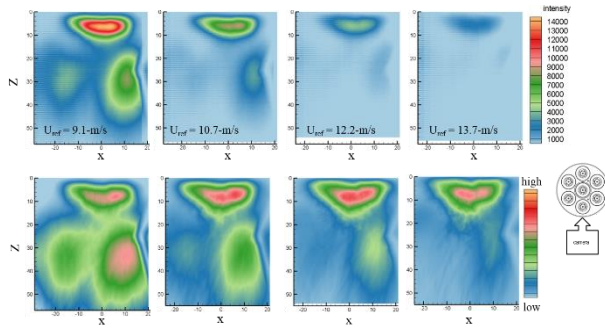


Figure 8: Mean C_2^* signal statistics from the high speed camera, showing variation based on cold flow reference velocity, which increases from left to right. Top row: mean signal, same scale. Bottom row: signal RMS, scaled independently.

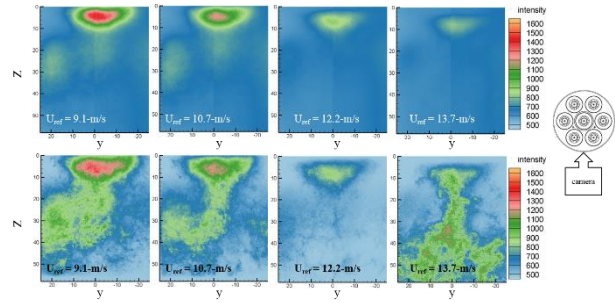


Figure 9: Mean C_2^* signal statistics from the ICCD camera, showing variation based on cold flow reference velocity, which increases from left to right. Top row: mean signal, same scale. Bottom row: signal RMS, scaled independently.

3.2.2 Flame spectroscopy

Figure 10 provides a few snapshots of individual spectra taken near the dump plane along $y = 0$, each scaled independently. Although each spectrum is somewhat noisy, we can generally see the OH peak, near 313-nm, and the CH peak near 430-nm. We can occasionally also see the C_2 peaks at 470-nm and 515-nm. Given that OH and CH peaks are seen most of the time, we are working to derive field maps as a function of position that show the average peak areas of OH and CH from the 10 spectra. Figure 11 shows a series of scatter plot maps of OH on the left and CH on the right for the lowest reference velocity condition. There are three maps, each showing the field at a different axial location, top, center, and bottom. The top height is located near the dome exit, and the bottom is farthest downstream. There is a small amount of overlap between the three heights. The maps are consistent with what we observe from the chemiluminescence images, which show more signal near the dump plane near $y = 0$. Unlike the images, though, these maps reflect an outward expansion of signal, which is more like a spray would behave. Most of the signal is gone by the midpoint, roughly 25-mm downstream. OH persists farther downstream than does CH. We hope to develop maps such as these to get a qualitative sense of speciation within the combustor.

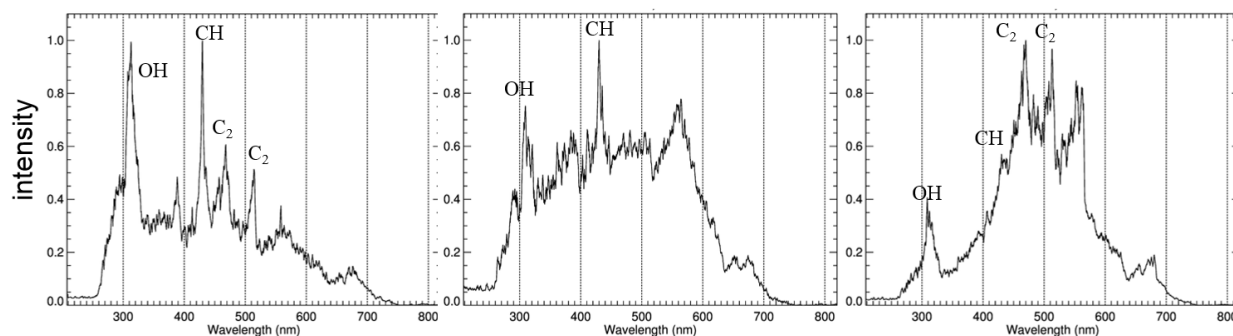


Figure 10: Sample spectra obtained using the spectrometer that show variation in species observed.

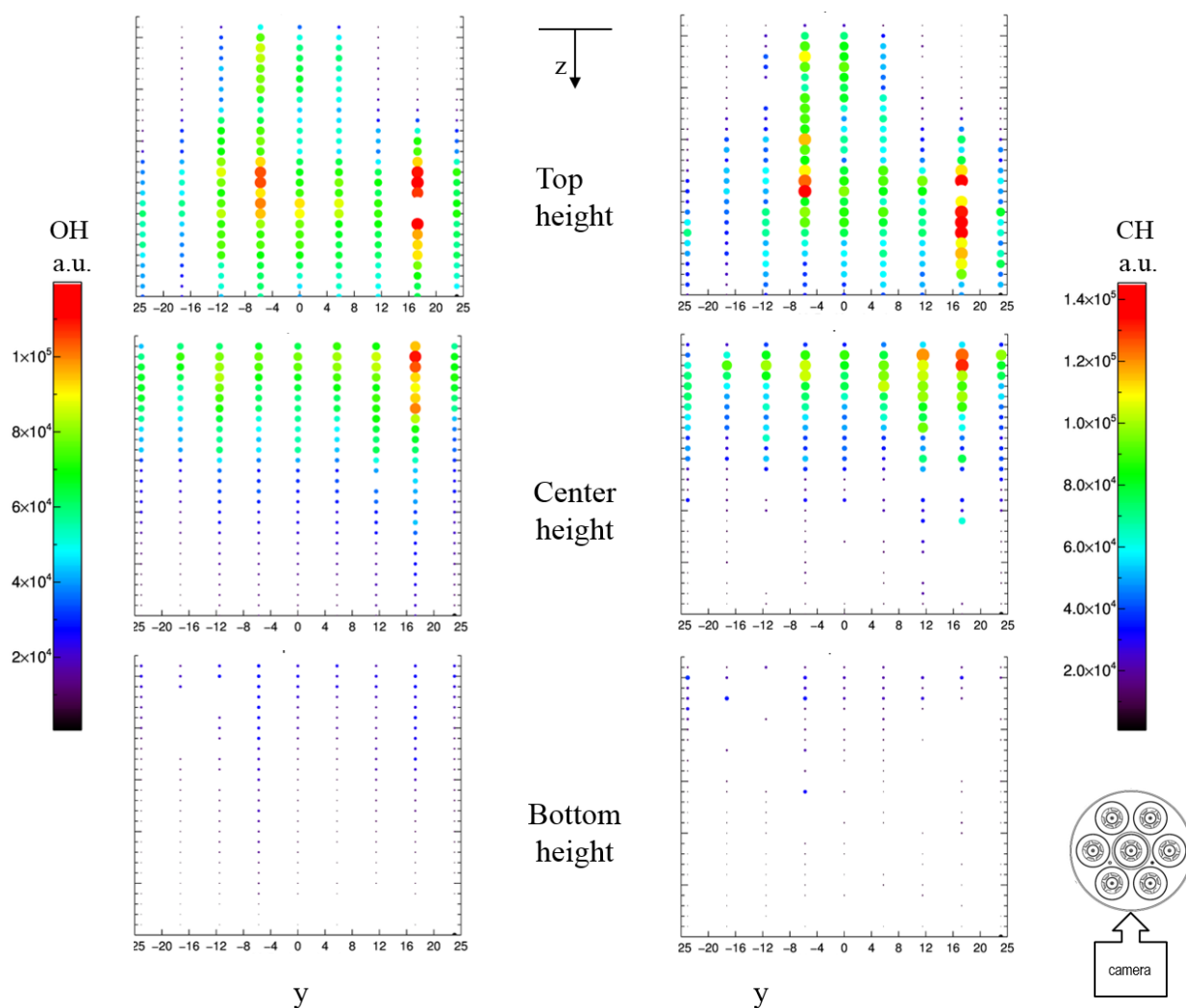


Figure 11: Species maps for OH (left) and CH (right) derived from the spectra obtained for the lowest reference velocity condition.

4. Summary

We presented data from our most recent parametric tests to characterize the flow field of a NASA 7-point LDI injector having a counterclockwise 60° center swirler surrounded by six clockwise 52° swirlers. The data included 2D non-combusting velocity fields and chemiluminescence data in the form of C₂* imaging and flame spectra. We saw from species imaging that for a given air flow rate, the chemiluminescence signal increases with increasing fuel flow rate under fuel-lean conditions. We also saw that at fixed equivalence ratio, the chemiluminescence signal decreases with increasing air flow rate (reference velocity). Continuing work for this configuration will include species mapping via flame spectra, analysis of the dynamic pressures, and combustion gas sample analysis.

5. Acknowledgements

This work was supported by the Transformational Tools and Technologies Project under the NASA Aeronautics Research Mission Directorate.

6. References

- [1] ZH. He, K. M. Tacina, C.-M. Lee, R.R. Tacina, P. Lee, Paper 070IC, 8th U.S. National Combustion Meeting, 2013.
- [2] R. Tacina, P. Lee, and C. Wey, A lean-direct-injection combustor using a 9 point swirl-venturi fuel injector, ISABE-2005-1106, 2005.
- [3] R. Tacina, C.-P. Mao, and C. Wey, AIAA-2004-0135, 2004.
- [4] C.-M. Lee, K.M. Tacina, and C. Wey, ISABE-2007-1270.
- [5] Y.R. Hicks, K.M. Tacina, R.C. Anderson, S.A. Tedder, A comparison of flow fields generated by varying swirler configurations in a 7-point lean direct injector array, 2016 Spring Technical Meeting, Central States Section of the Combustion Institute, Paper 145IC-0035.
- [6] Y.R. Hicks, K.M. Tacina, R.C. Anderson, Effect of air swirler configuration on lean direct injector flow structure and combustion performance with a 7-point lean direct injector array ISABE-2017-22620.
- [7] K. Ajmani, H.C. Mongia, P. Lee, Evaluation of CFD best practices for combustor design: Part I – non-reacting flows, Paper AIAA 2013-1144, 2013.